On the use of Matrix Information Geometry for Polarimetric SAR Image Classification

Pierre Formont, Jean-Philippe Ovarlez, Frédéric Pascal

On the use of Matrix Information Geometry for Polarimetric SAR Image Classification

Pierre Formont[1,2], Jean-Philippe Ovarlez[1], and Frédéric Pascal[2]

[1] French Aerospace Lab, ONERA DEMR/TSI, France
[2] E3S-SONDRA, Supélec, France

Abstract. Polarimetric SAR images have a large number of applications. To extract a physical interpretation of such images, a classification on their polarimetric properties can be a real advantage. However, most classification techniques are developed under a Gaussian assumption of the signal and compute cluster centers using the standard arithmetical mean. This paper will present classification results on simulated and real images using a non-Gaussian signal model, more adapted to the high resolution images and a geometrical definition of the mean for the computation of the class centers. We will show notable improvements on the classification results with the geometrical mean over the arithmetical mean and present a physical interpretation for these improvements, using the Cloude-Pottier decomposition.

1 Introduction

Large-scale observation of the Earth is achieved thanks to two main methods : observation *via* optical systems and observation *via* radar systems. The latter offer two advantages over the former: the independence from the illumination of the area to be observed and the ability to go through clouds. Thus, data can be acquired whatever the time of day and whatever the weather. These properties have led radar systems to be used in numerous applications in both the civilian and the military domain, such as ship detection, iceberg detection, land cover classification etc. The only practical technique which achieves high spatial resolution is the Synthetic Aperture Radar (SAR) and therefore, most if not all, active imaging radars are SAR.

A SAR measures both the phase and the amplitude of the backscattered signal for each resolution cell. Thus, pixels of the resulting image are complex. POLarimetric SAR (POLSAR) systems are able to polarize the waves in emission and in reception along several orthogonal polarizations. For each resolution cell, there are thus several measurements corresponding to the different combinations in polarization.

The random distribution of scatterers inside a resolution cell leads to the radar measurement being modeled by a random variable. As each resolution cell contains a large number of scatterers, the Central Limit Theorem implies that the radar measurement is Gaussian distributed. Thus, POLSAR data is usually modeled by a multivariate complex Gaussian distribution.

The interactions between polarisation channels can be related to the physical information of the observed scene. Obtaining information on these interactions allows to obtain information about the physical processes that take place when an electromagnetic wave hits an object. The random nature of these interactions can be studied using their second order moment, called the covariance matrix.

As previously mentioned, polarimetric SAR images can be used for several applications, in particular land cover classification. Therefore, polarimetric SAR images classification is an active area of research. Two main approaches appeared in the corresponding literature. The first approach is to classify pixels thanks to their physical characteristics. Several matrix decompositions have been proposed: coherent decompositions, based on the scattering matrix, like the Cameron decomposition [6] or the Krogager decomposition [14], in order to characterize pure scatterers. The distributed scatterers have been studied thanks to incoherent decompositions, i.e. decompositions of the covariance matrix. Freeman et al. [10] proposed such a decomposition. In [7], Cloude et al. proposed the $H - \alpha$ decomposition, based on the eigendecomposition of the covariance matrix. The second approach is to classify the images based on their statistical properties: Kong et al. [13] derived a distance measure for single-look complex polarimetric SAR data, which has been extended by Yueh et al. [23] and van Zyl et al. [20] for normalized complex POLSAR data. A distance measure for the multi-look complex case has been proposed by Lee et al. in [16], based on the complex Wishart distribution of the clutter covariance matrix under the Gaussian assumption.

However, recent POLSAR acquisition systems are now able to acquire very high resolution images, up to decimetric resolution. Thus, there are fewer scatterers in each resolution cell and their number varies from one resolution cell to the other. This leads to a higher heterogeneity, especially in urban areas. Thus, the backscattered signal can no longer be modeled as a Gaussian process. One commonly used fully polarimetric non-Gaussian clutter model is the Spherically Invariant Random Vector (SIRV) model. The polarimetric clutter is no longer modeled as a Gaussian process but as the product of a Gaussian process and a random variable. This random variable, called *texture*, represents the local variations of power, hence the heterogeneity.

2 State of the Art

2.1 SAR signal statistics

Gaussian assumption In order to reduce the speckle noise in early SAR systems, a common approach was to average several indepedent estimates of the reflectivity of each resolution cell. The quantities in each pixel of the resulting so-called multilook image are therefore Gaussian-distributed. To obtain the covariance matrix of a polarimetric scattering vector $\mathbf{k}$, corresponding to a pixel of

the image, it is necessary to employ an estimation scheme, as the covariance matrix cannot be computed directly. Several samples $(\mathbf{k}_1, ...\mathbf{k}_N)$ are drawn from the immediate neighbourhood of the pixel under consideration, with the assumption that they are independent and identically distributed (i.i.d.). A boxcar neighbourhood is generally used for this. The Maximum Likelihood Estimate of the covariance matrix $\mathbf{M}$ is then the so-called Sample Covariance Matrix (SCM), given by the following equation:

$$\widehat{\mathbf{M}}_{SCM} = \frac{1}{N}\sum_{i=1}^{N}\mathbf{k}_i\mathbf{k}_i^H \tag{1}$$

with $\mathbf{k}_1, ..., \mathbf{k}_N \sim \mathcal{N}(0, \mathbf{M})$ and ^{H} denotes the tranpose conjuguate operator.

Polarimetric non-Gaussian model Yao [22] first introduced Spherically Invariant Random Vectors for estimation and detection in communication theory. A SIRV is a compound Gaussian vector, defined as the product of a positive scalar random variable τ and a m-dimensional complex circular Gaussian vector, $\mathbf{x}$, with m the number of configurations of polarizations. Then the target vector $\mathbf{k}$ can be rewritten as:

$$\mathbf{k} = \sqrt{\tau}\mathbf{x} \tag{2}$$

By writing $\mathbf{k}$ this way, the polarimetric information, which is the information about the interactions between the polarimetric channels, is separated from the power information. Indeed, the texture τ is a random variable. Its value changes randomly from cell to cell: it represents the local variations of power that are characteristics of the heterogeneity. $\mathbf{x}$, then, contains only information about the phase differences between polarizations channels: polarimetric information.

In the SIRV model, the Probability Density Function (PDF) of the texture τ is not explicitly specified. This allows for a large class of stochastic processes to be described. For example, the Gaussian case can be obtained with a Dirac pdf for τ. The K distribution, which has been successfully used to describe radar signal in heterogeneous areas, can be modeled with a Gamma-distributed texture.

Considering a deterministic texture, Gini et al. derived in [11] the Maximum Likelihood (ML) estimate of the covariance matrix $\mathbf{M}$. It is the fixed point of the following function:

$$f\left(\widehat{\mathbf{M}}_{FP}\right) = \frac{m}{N}\sum_{i=1}^{N}\frac{\mathbf{k}_i\mathbf{k}_i^H}{\mathbf{k}_i^H\widehat{\mathbf{M}}_{FP}\mathbf{k}_i} \tag{3}$$

This estimate is therefore called the Fixed Point Estimate (FPE). In [8], Conte et al. extended the validity of the FPE as an approximate ML estimate for the case of stochastic texture. In [18], Pascal et al. have proven that the FPE

as a solution to Eq. (3) exists and is unique up to a scalar factor. They also proved in [18] that it is unbiased, consistent and asymptotically Wishart-distributed.

The main advantage of the FPE over the SCM for polarimetric classification is the removal of the power information. Indeed, by replacing $\mathbf{k}_i$ by $\sqrt{\tau_i}\mathbf{x}_i$ in Eq. (3), the expression of the FPE becomes:

$$\widehat{\mathbf{M}}_{FP} = \frac{m}{N}\sum_{i=1}^{N}\frac{\mathbf{x}_i\mathbf{x}_i^H}{\mathbf{x}_i^H\widehat{\mathbf{M}}_{FP}\mathbf{x}_i} \tag{4}$$

The FPE is then independent from the random fluctuations of power modeled by the texture and depends only on the information stored in the vector $\mathbf{x}$, which is the polarimetric information. This way, classification methods employed on the covariance matrix estimate are more likely to properly exploit the polarimetric information with the FPE than with the SCM.

2.2 Wishart classifier

In [15], Lee et al. proposed an unsupervised classification method based on the complex Wishart distribution of the covariance matrix under Gaussian assumption for the speckle. A distance measure between a class center $\mathbf{C}$ and the covariance matrix of a pixel $\widehat{\mathbf{M}}$, called the Wishart distance measure is derived:

$$\mathrm{d}_W\left(\widehat{\mathbf{M}},\mathbf{C}\right) = \ln|\mathbf{C}| + \mathrm{Tr}\left(\mathbf{C}^{-1}\widehat{\mathbf{M}}\right) \tag{5}$$

where $|.|$ is the matrix determinant. The Wishart distance measure is not strictly a distance as it is not symmetrical. Its purpose is to measure the distance between a Wishart-distributed covariance matrix and a cluster center, see [15] for more details on how it is obtained.

This distance is used in a standard K-means classification scheme to assign pixels to classes until a stopping criterion is met. The purpose of the K-means algorithm is, given a set of observations, to partition these observations into a given number of clusters (or classes) in order to minimize the within-cluster sum of squares. It is comprised of two steps: an assignement step, where each observation is assigned to the closest class according to a specific distance, and an update step where the class centers are updated according to the observations switching classes.

The algorithm of the Wishart classifier is then:

1. Initially classify the image with the Cloude-Pottier decomposition [7].
2. Compute the class centers $\mathbf{C}_i = \frac{1}{p_i}\sum_{j=1}^{p_i}\widehat{\mathbf{M}}$, where p_i is the number of pixels in class i .
3. Reassign pixels to the corresponding class thanks to Eq. (5)
4. Repeat steps 2-3 until a stopping criterion is met.

2.3 Information geometry

Until now, all classical approaches compute the class centers as the empirical arithmetic mean $\mathbf{C}_i = \dfrac{1}{p_i}\displaystyle\sum_{j=1}^{p_i}\widehat{\mathbf{M}}$. The problem is that the space of covariance matrices, $\mathcal{P}(m)$, *ie* hermitian definite positive matrices is not a euclidean space. It has the structure of a Riemannian manifold and while the matrix obtained by computing the arithmetical mean stays inside $\mathcal{P}(m)$, it is not the proper definition of the mean as the barycenter in this space. Moakher [17] and Barbaresco (notably [3], [4] and [5]) have proposed methods to compute the barycenter of several matrices in $\mathcal{P}(m)$. More recently, Devlaminck illustrated in [9] the dangers in using a Euclidean definition of the mean for polarized light. When computing the mean Stokes parameters, which are parameters describing the polarization state of an electromagnetic wave, of a horizontally linear polarized light passing through a perfect linear polarizer with a rotating axis of polarization, the resulting mean vector was partially polarized. Using a Riemannian distance, the mean Stokes vector was fully polarized, which was the expected behavior.

Wang et al. also presented a mean-shift clustering technique using similar techniques for polarimetric SAR data in [21], which yields very interesting results. However, they do not address the issue of non-Gaussianity when considering the covariance (or coherency) matrix of the pixels.

We recall here how to obtain the Riemannian expression of the mean and a Riemannian distance in $\mathcal{P}(m)$.

The metric is defined on this space by:

$$\mathrm{d}s^2 = \mathrm{Tr}\left(\left(\mathbf{M}^{-1}\left(\mathrm{d}\mathbf{M}\right)\right)^2\right) \tag{6}$$

which leads to the following distance:

$$d_G(\mathbf{A},\mathbf{B}) = \left\|\log\left(\mathbf{A}^{-1/2}\mathbf{B}\mathbf{A}^{-1/2}\right)\right\| = \sum_{i=1}^{N}\log(\lambda_i) \text{ with } |\mathbf{B}-\lambda\mathbf{A}| = 0 \tag{7}$$

The correct expression of the mean for class c_l is then:

$$\mathbf{M}_{\omega_l} = \underset{\mathbf{M}_\omega\in\mathcal{P}(m)}{\arg\min}\sum_{k=1}^{K}\left|\left|\log\left(\mathbf{M}_k^{l\,-1/2}\,\mathbf{M}_\omega\,\mathbf{M}_k^{l\,-1/2}\right)\right|\right|_F^2 \tag{8}$$

There is no analytical solution for $K > 2$ but a gradient descent method leads to the following iterative procedure for the solution:

$$\mathbf{M}_k = \left(\mathbf{M}_{k-1}^{1/2}\right)^H \exp\left(\epsilon\sum_{i=1}^{K}\log\left(\left(\mathbf{M}_{k-1}^{-1/2}\right)^H\,\mathbf{M}_i^l\,\mathbf{M}_{k-1}^{-1/2}\right)\right)\mathbf{M}_{k-1}^{1/2} \tag{9}$$

3 Simulations

3.1 Construction of the simulations

Toeplitz matrices are regurlaly used in radar processing to model specific configurations, such as Space-Time Adaptive Processing. Polarimetric covariance matrices are then generated as Toeplitz matrices for this reason and for convenience. We could also have used matrices obtained from real data but results would be similar. Complex Toeplitz matrices are of the form:

$$\begin{pmatrix} 1 & \rho & \rho^2 \\ \overline{\rho} & 1 & \rho \\ \overline{\rho^2} & \overline{\rho} & 1 \end{pmatrix} \tag{10}$$

with $\rho \in \mathbb{C}$.

Four matrices are used to generate polarimetric radar data. In each quadrant, random scattering vectors are generated out of one of the four matrices. Each quadrant is divided in four subquadrants. In each of the subquadrants, scattering vectors are drawn along a K distribution with a different shape parameter from subquadrant to subquadrant. Fig. 1 illustrates this process:

The K distribution results from the multiplication of a multivariate Gaussian random vector with a Gamma-distributed random variable, described by the shape parameter λ. When the shape parameter λ of the Gamma distribution tends to infinity, it converges to a Gaussian distribution. Therefore, shape parameters $\lambda = \begin{pmatrix} 0.5 & 1 & 5 & 50 \end{pmatrix}$ have been chosen in order to have areas that are clearly non Gaussian and others that are close to being Gaussian-distributed. The images have additionaly been multiplied by a uniformly distributed power, to model the heterogeneity. The ρ coefficient has been chosen for each Toeplitz matrix among the following coefficients:

$$\rho \in \begin{bmatrix} 0.8003 + 0.1419i \\ -0.4404 - 0.1645i \\ 0.4715 - 0.1927i \\ 0.1576 - 0.9706i \end{bmatrix}.$$

Those coefficients were chosen to ensure covariance matrices are as diverse as possible.

3.2 Standard Wishart classifier

On Fig. 2 is represented the power of each pixel. It is visually impossible to separate the areas from this image alone as several areas built from different distributions have the same appearance.

The results of the standard Wishart classifier presented on section 2.2 with the use of the SCM are displayed on Fig. 3. The number of classes was set to 4. Pixels were initially assigned to classes in a random uniform way. The algorithm

$\sim \mathcal{K}(\mathbf{M}_1, \lambda_1)$	$\sim \mathcal{K}(\mathbf{M}_1, \lambda_2)$	$\sim \mathcal{K}(\mathbf{M}_2, \lambda_1)$	$\sim \mathcal{K}(\mathbf{M}_2, \lambda_2)$
$\sim \mathcal{K}(\mathbf{M}_1, \lambda_3)$	$\sim \mathcal{K}(\mathbf{M}_1, \lambda_4)$	$\sim \mathcal{K}(\mathbf{M}_2, \lambda_3)$	$\sim \mathcal{K}(\mathbf{M}_2, \lambda_4)$
$\sim \mathcal{K}(\mathbf{M}_3, \lambda_1)$	$\sim \mathcal{K}(\mathbf{M}_3, \lambda_2)$	$\sim \mathcal{K}(\mathbf{M}_4, \lambda_1)$	$\sim \mathcal{K}(\mathbf{M}_4, \lambda_2)$
$\sim \mathcal{K}(\mathbf{M}_3, \lambda_3)$	$\sim \mathcal{K}(\mathbf{M}_3, \lambda_4)$	$\sim \mathcal{K}(\mathbf{M}_4, \lambda_3)$	$\sim \mathcal{K}(\mathbf{M}_4, \lambda_4)$

Fig. 1. Structure of the simulated image

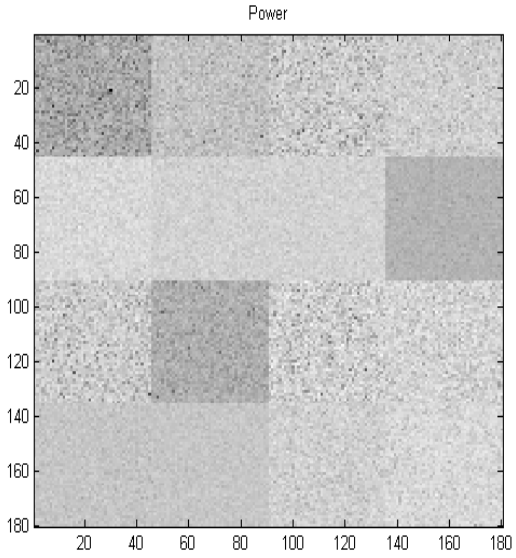

Fig. 2. Power image

was stopped when less than 5 percent of the pixels switched classes from one iteration to the next.

The influence of the power over the polarimetric information with this estimate can be clearly identified. Areas with the same power - the same shade of grey in Fig. 2 - are assigned to the same class, even when they originate from a different distribution.

However, as can be seen on Fig. 4, the same classification method using the FPE yields a result closer to what was expected. Areas are clearly separated thanks to their difference in the covariance matrix rather than their difference in power. However, the two separate areas on the right side of the image are identified as one class while they have been constructed as two separate classes. Surprisingly, when investigating the distances (in Frobenius norm, among others) between the 4 initial matrices, the two matrices corresponding to the right side areas of the image are not particularly close. This is most likely a consequence of the random initialisation as with other random initialisations, the results were different. Most of the time, classes were correctly separated with the Fixed Point Estimate but still, there are cases where the classification fails. Our assumption is that the computation of the class centers with the euclidean definition of the mean groups pixels that should not be grouped and in most cases, it has little to no impact on the classification results. But sometimes, the errors due to this miscalculation of the mean may have a strong impact on the end results. Using the geometric definition of the mean can alleviate this effect.

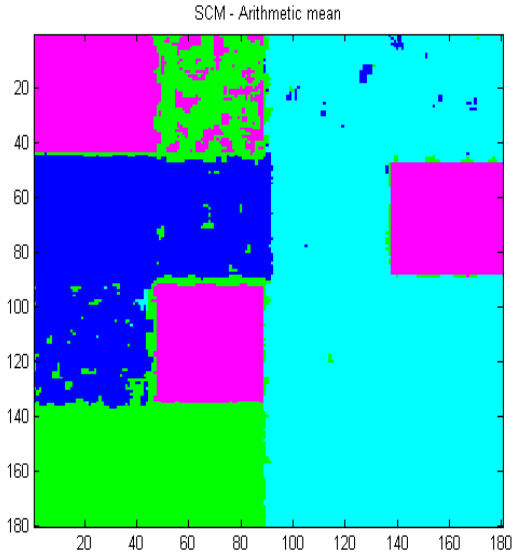

Fig. 3. Standard Wishart classification with the SCM

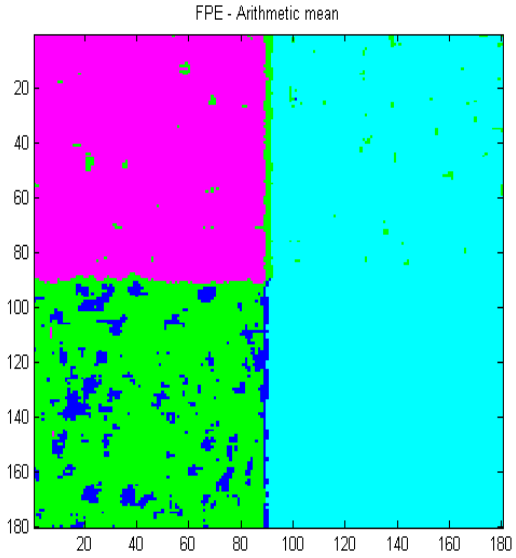

Fig. 4. Standard Wishart classification with the FPE

3.3 Information geometry

Fig. 5 presents the results of the classification process using the FPE and the geometrical mean, instead of the standard arithmetical mean, with the same initialization as Fig. 3 and Fig. 4. It is clear that the use of the geometrical mean allowed for a better classification as the four initial quadrants are crealy visible on the end results. However, one must note that the initialization still plays a strong part. Some configurations, not shown here, lead to a failure of the classification process, even when using the geometrical mean.

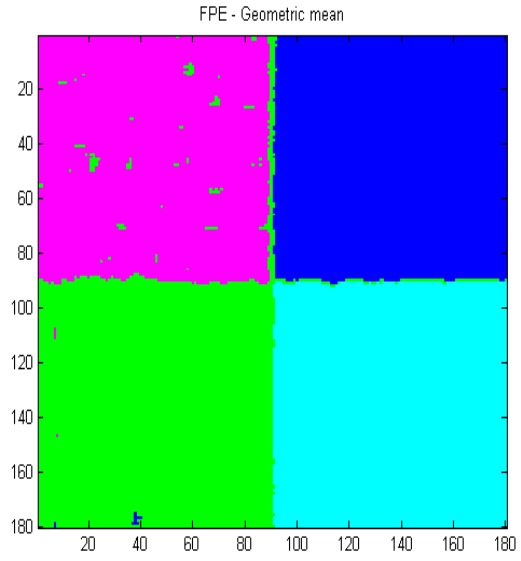

Fig. 5. Wishart classification with the FPE and the geometrical mean

4 Results on real data

Simulations have presented a notable improvement on the classification accuracy in the polarimetric sense, as they showed that even when using the SIRV model, which is more adapted to describe non-Gaussian clutter, large areas of the image could be misclassified when using the incorrect euclidean definition of the mean. This calls strongly for an application of the geometry of information on a real scene, where a lot of polarimetric mechanisms can be encountered and where the opportunities for misclassification abound. This is why the algorithms used in the simulations in Section 3 have been applied on a data set acquired by the ONERA RAMSES system in the region of Brétigny, France. This image,

presented on Fig. 6 has a resolution of approximately 1.3 meters in both range and azimuth and has been acquired in X-band with a 30° incidence angle.

4.1 Classification results

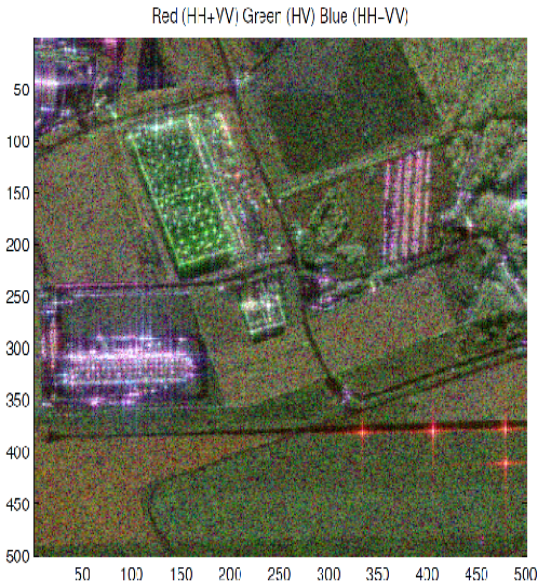

Fig. 6. Real polarimetric image in the Pauli basis.

Wishart distance measure The image on Fig. 6 is represented in the Pauli basis : blue for the $\|HH + VV\|$ component, red for the $\|HH - VV\|$ and green for the $\|HV\|$ component. This decomposition allows for a very quick assessment of the polarimetric mechanisms in an image. Indeed, a strong $\|HH + VV\|$ component is characteristic of scattering over a surface, a strong $\|HH - VV\|$ component indicates double-bounce scattering and a strong $\|HV\|$ component indicates volume scattering, which is generally present in forested areas. However, color mixtures are very subject to interpretation and should be handled carefully.

In this image, a lot of polarimetric diversity is present. Two large buildings can be observed in the left part of the image, one in purple and white, the other in green. Smaller buildings and several fields are scattered among the image. A forested area is present on the right side. On the lower right side, four corner reflectors have a strong signal in red.

Applying the Wishart classifier of Sect. 2.2 with the Fixed Point Estimate, the Wishart distance measure and the arithmetical mean yields the classification results presented on Fig. 7.

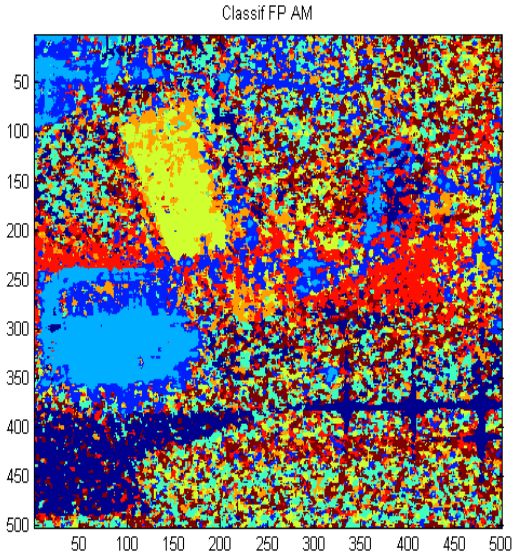

Fig. 7. Wishart Classifier with FPE, arithmetical mean and Wishart distance measure.

The two large buildings are effectively separated from the rest of the image. The yellow class consists solely of one the large buildings and small patches near some of the smaller buildings. There are also small patches of the orange class near this building and some of the smaller ones. The other large building is represented by the two classes : the medium blue and the light blue class. Those classes are also found on the smaller buildings and on the urban area of the top left. The teal and red classes seem to be present in the more natural areas.

The last class, in dark blue, is more difficult to interpret because it contains natural areas like the field in the lower left corner and the corner reflectors of the lower right who have a very strong unambiguous double-bounce return. The arithmetical mean of the class centers leads to a bias in their expression and pixels with quite different polarimetric are assigned to the same class because of this. Using the correct geometrical expression of the mean between covariance matrices should hopefully correct this and properly separate pixels.

Fig. 8 represents the classification results with the Fixed Point Estimate, the Wishart distance measure and the geometrical mean. As can be seen on this image, the classification accuracy is improved concerning the dark blue class

of Fig. 7. It consists now almost exclusively of the pixels corresponding to the corner reflectors with a few patches left on the field of the lower left corner. The medium blue class appears sharper as well in both the urban area of the top left, the small building in the center of the image - that was not identifiable in Fig. 7 - and the parking lot on the right side.

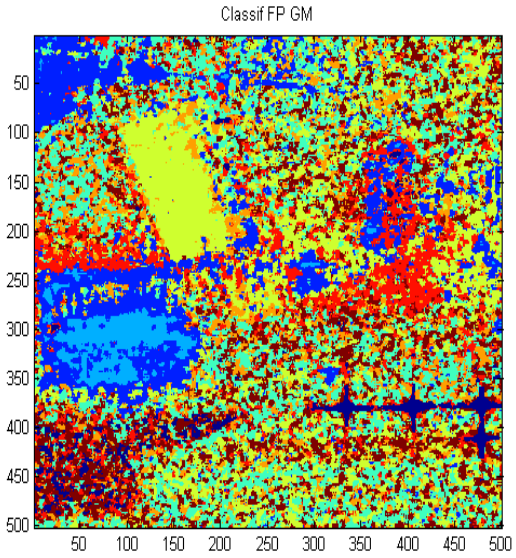

Fig. 8. Wishart Classifier with FPE, geometrical mean and Wishart distance measure.

Those classification results were obtained with a 5-by-5 sliding window for the estimation of the covariance matrix. If we increase the size of this sliding window to a 15-by-15 window, the classification leads to the results presented in Fig. 9. With the geometrical mean, the corner reflectors are separated in the yellow class, which contains only them. The field of the lower left corner is in the separate red class, along with a few patches scattered among the image and some pixels around the centers of the corner reflectors. The two large buildings are in two separate class containing only them as well, the teal and medium blue classes. The brown class gathers all the remaining pixels belonging to urban or man-made elements of the scene.

Geometrical distance The distance of Eq. (7) can also be used instead of the Wishart distance measure to reassign the pixels at each iteration. Classification results using the geometrical distance are presented on Fig. 10.

In that case, we observe again a better performance of the geometrical mean over the arithmetical mean with regards to the polarimetric classification. Al-

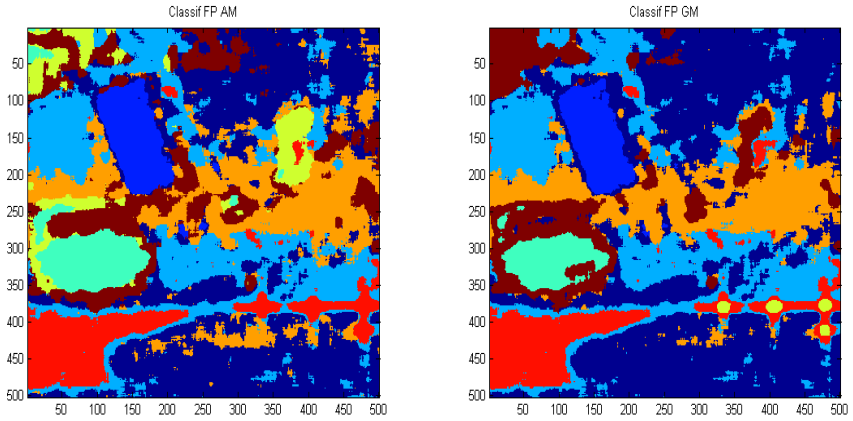

(a) Wishart Classifier: FPE, AM, Wishart distance measure.

(b) Wishart Classifier: FPE, GM, Wishart distance measure.

Fig. 9. Wishart Classifier: FPE, Wishart distance measure, 15-by-15 sliding window.

though, with the AM, the algorithm is able to discriminate between the large buildings and the rest of the image, the shapes of both the small and the large buildings are much better outlined using the GM. The urban area of the top left corner and the parking lot are correctly classified in the same class as other buildings. The green class consists solely of the very tip of the corner reflectors.

However, in both cases, all the other pixels are more or less assigned to the same class which shows that the geometrical distance may not be pertinent for use in polarimetric classification.

4.2 Polarimetric interpretation

One of the most commonly used ways to interpret the underlying polarimetric mechanisms in a polarimetric SAR image is the Cloude-Pottier decomposition [7]. This decomposition relies on the eigendecomposition of the covariance matrix, under the assumption that each resolution cell contains a dominant scattering mechanism. The eigendecomposition of the covariance matrix yields the eigenvalues λ_i and the eigenvectors u_i. The eigenvectors can be represented as:

$$u_i = \begin{bmatrix} cos\alpha_i e^{j\phi_i} \\ sin\alpha_i cos\beta_i e^{j(\delta_i+\phi_i)} \\ sin\alpha_i sin\beta_i e^{j(\gamma_i+\phi_i)} \end{bmatrix} \tag{11}$$

where $\alpha_i, \beta_i, \delta_i, \phi_i$ are angles related to the wave propagation (see [7] for more details).

From the eigenvalues, we define: $p_i = \dfrac{\lambda_i}{\sum_{k=1}^{m} \lambda_k}$.

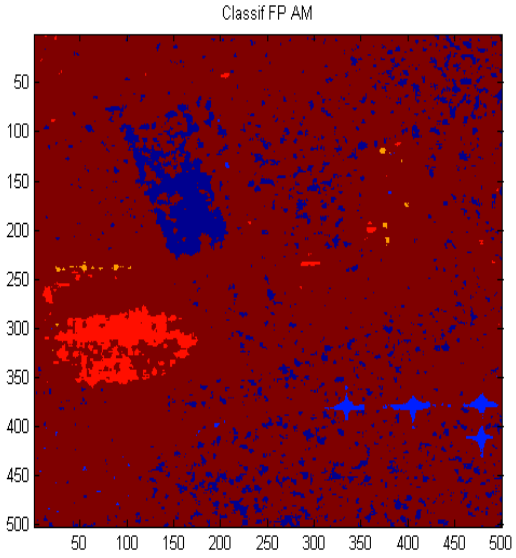

(a) Wishart Classifier: FPE, AM, geometrical distance.

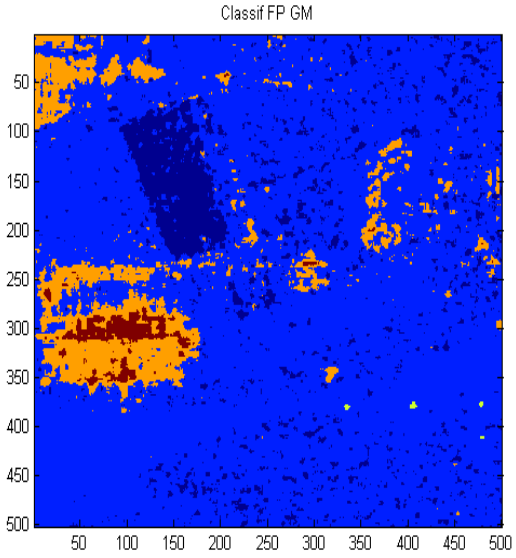

(b) Wishart Classifier: FPE, GM, geometrical distance.

Fig. 10. Wishart Classifier: FPE, geometrical distance.

Two physical parameters are then extracted from the eigenvalues and the eigenvectors:

- the entropy H: it characterizes the degree of chaos inside the resolution cell. It takes values between 0 and 1. If the entropy is low, there is indeed a dominant polarimetric mechanism. When the entropy increases, it indicates there are other scattering mechanisms inside the cell which are not negligible. When it is close to 1, it means there is no dominant mechanism inside the cell, the contribution of the several mechanisms is equivalent. It is given by:

$$H = -\sum_{i=1}^{m} p_i \log_m(p_i) \tag{12}$$

- the α angle: this parameter is not related to any physical angle but gives an indication on the type of the dominant mechanism. It takes values between 0 and 90 degrees. It is given by:

$$\alpha = \sum_{i=1}^{m} p_i \alpha_i \tag{13}$$

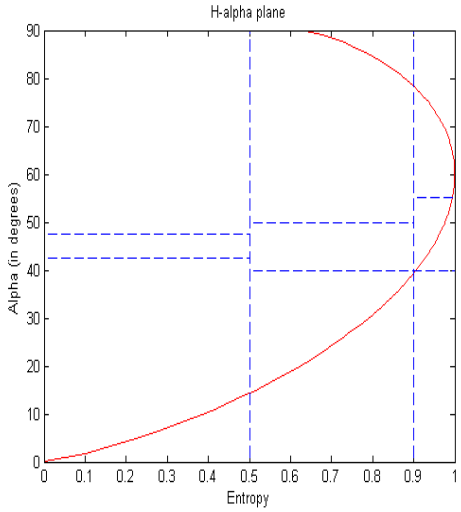

Fig. 11. $H - \alpha$ plane

The underlying scattering mechanism for each pixel can then be characterized knowing its parameters H and α and their position in the $H-\alpha$ plane represented in Fig. 11. The red curve represents the limit of entropy-α couples that are physically possible. The dotted blue lines roughly delimit areas where different

scattering mechanisms take place. These boundaries are not set in stone but offer a rather quick and visual separation between mechanisms.

The repartition of the pixels in each class in the $H - \alpha$ plane after the classification ended are presented on Fig. 12 for the arithmetical mean and on Fig. 13 for the geometrical mean.

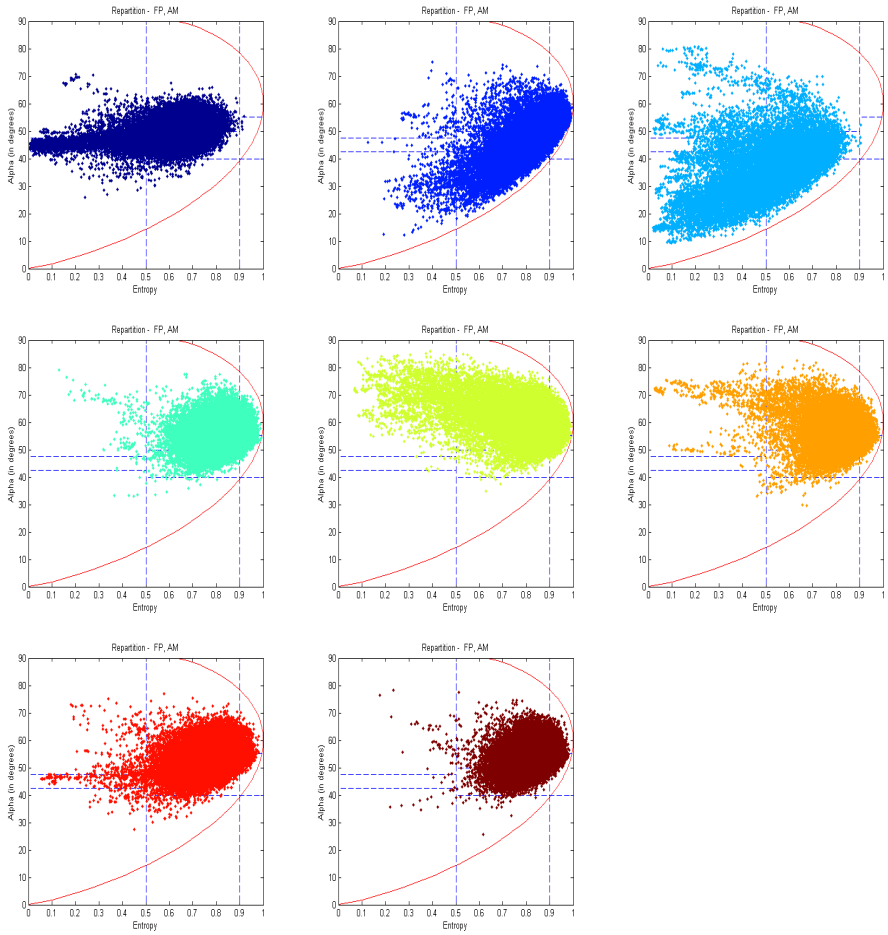

Fig. 12. Repartition in the $H - \alpha$ plane after classification, AM.

If we take a closer look at the most pertinent classes, like the dark and light blue classes, we can see that the pixels belonging to these classes appear to be more clustered. For the dark blue class, the range in both alpha and entropy is reduced, which means that the pixels belonging to this class are more similar in the polarimetric sense. This was expected as the classification appeared to refine the class around the corner reflectors. For the other classes, the deviations

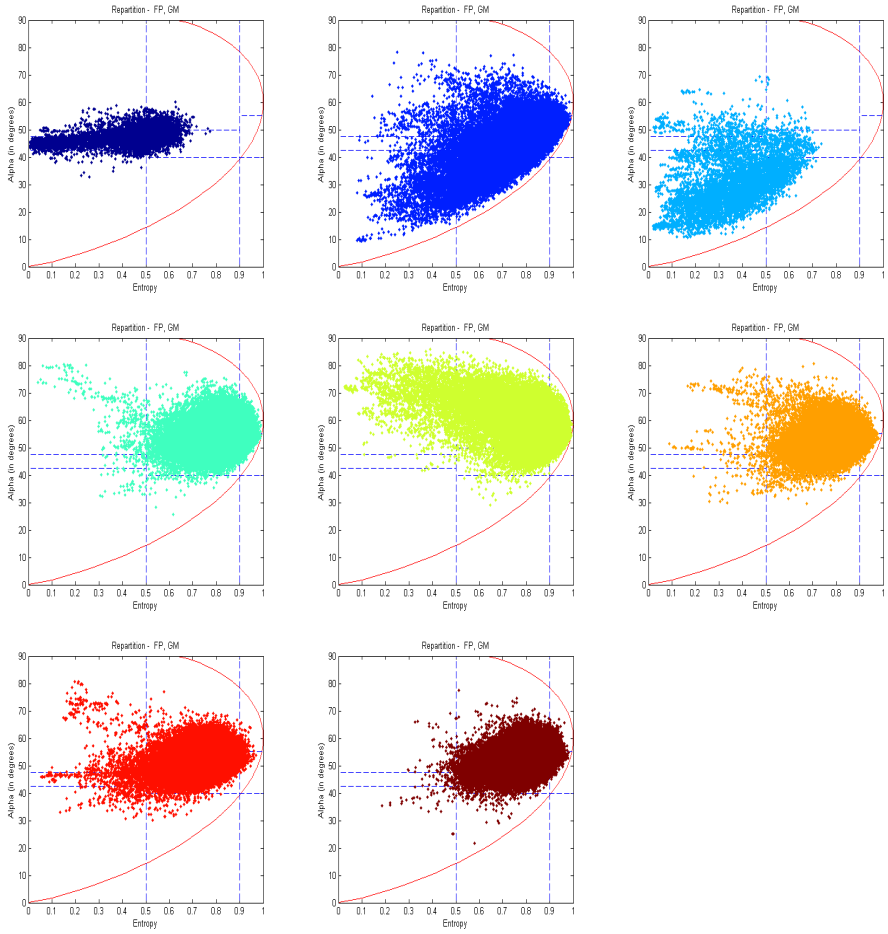

Fig. 13. Repartition in the $H - \alpha$ plane after classification, GM.

in alpha and entropy are roughly the same using either one of the means. We can take a look at the repartition using the 15-by-15 sliding window, represented on Fig. 14. Only the red and green classes are represented because they are the only classes relevant to the corner reflectors. We have seen that using the 15-by-15 sliding window, the corner reflectors were separated in a unique class with the geometrical mean: the green class. Fig. 14 shows these pixels all have a low entropy and an α angle between 40 and 50 degrees, which is coherent with the response of a corner reflector.

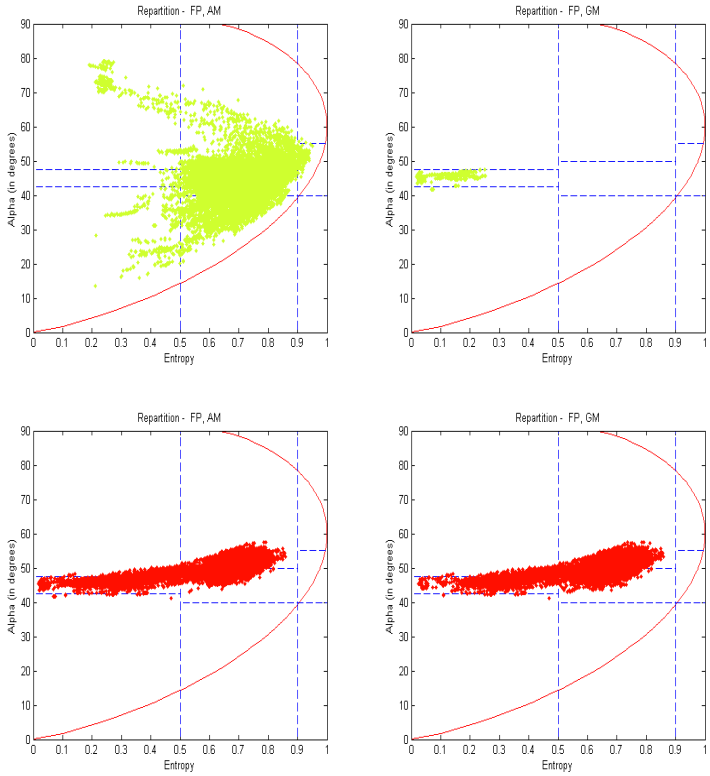

Fig. 14. Repartition in the $H - \alpha$ plane after classification, AM and GM, 15x15.

5 Conclusion

This paper presented a method for polarimetric SAR data classification using information geometry. It relies on a rigorous definition of the metric on the space of Hermitian semi-definite positive matrices.

The signal was described using the non-Gaussian SIRV model. In this model, the Approximate Maximum Likelihood of the covariance matrix is the Fixed Point Estimate. It is independent of the texture PDF and thus allows to discriminate between matrices only on their polarimetric properties - the phase relationships between the polarimetric channels - rather than their power.

Classifications were performed on simulated images with parts of the image Gaussian-distributed and other parts non-Gaussian distributed. Results on the SCM and its classification on the power were briefly recalled and improvements on classification with the FPE were presented when using the geometrical expression of the mean.

The algorithm was then applied to a real polarimetric image and results show that the classification was improved using the geometrical mean as classes

consisted of pixels more similar in the polarimetric sense, based on the ground truth and a physical interpretation thanks to the Cloude-Pottier decomposition. Differences on the results were noted when using different sizes for the sliding window used for the estimation of the covariance matrices. Binary partition trees [1] and expectation-maximization algorithm [12] have also been used in polarimetric SAR classification and could be more robust to the initialisation than the simple k-means algorithm. A k-means++ algorithm [2] could be used to alleviate this problem. On large images, the computation time can also become an issue so using Bregman ball trees [19] could potentially help with this aspect of the problem.

A distance derived from information geometry was also used instead of the standard Wishart distance measure to reassign pixels in the algorithm but results are not conclusive at this time.

The proposed method yields encouraging results but the end results remain too vague, especially on the natural areas. Combining the polarimetric information with the power information, which is removed here, could greatly help the visual aspect of the final images.

6 Acknowledgments

The authors would like to thank the DGA for funding this research.

References

1. C.; Salembier P. Alonso-Gonzalez, A.; Lopez-Martinez. Filtering and segmentation of polarimetric sar images with binary partition trees. *Geoscience and Remote Sensing Symposium (IGARSS), 2010 IEEE International*, 2010.
2. David Arthur and Sergei Vassilvitskii. k-means++: The advantages of careful seeding. Technical Report 2006-13, Stanford InfoLab, June 2006.
3. F. Barbaresco. Innovative tools for radar signal processing based on cartan's geometry of spd matrices and information geometry. *IEEE International Radar Conference*, 2008.
4. F. Barbaresco. Robust median-based stap in inhomogeneous secondary data : Frechet information geometry of covariance matrices. *2nd French-Singaporian SONDRA Workshop on EM Modeling, New Concepts and Signal Processing For Radar Detection and Remote Sensing*, 2010.
5. F. Barbaresco. Information geometry of covariance matrix: Cartan-siegel homogeneous bounded domains, mostow/berger fibration and frechet median. *MIG Proceedings, Springer*, 2012.
6. W L Cameron, N Youssef, and L K Leung. Simulated polarimetric signatures of primitive geometrical shapes. *IEEE Trans.-GRS*, 34(3):793–803, May 1996.
7. Shane R. Cloude and E. Pottier. An entropy based classification scheme for land applications of polarimetric SAR. *IEEE Transactions on Geoscience and Remote Sensing*, 35(1):68–78, January 1997.
8. E Conte, A De Maio, and G Ricci. Recursive estimation of the covariance matrix of a compound-Gaussian process and its application to adaptive CFAR detection. *IEEE Trans.-SP*, 50(8):1908–1915, August 2002.

9. V. Devlaminck and P. Terrier. Geodesic distance on non-singular coherency matrix space in polarization optics. *J. Opt. Soc. Am. A*, 27(3), 2010.
10. A Freeman and S Durden. A three component scattering model to describe polarimetric SAR data. *Radar Polarimetry*, 1748:213–225, 1992.
11. F. Gini and M.V. Greco. Covariance matrix estimation for CFAR detection in correlated heavy-tailed clutter. *Signal Processing*, 82(12):1847–1859, 2002.
12. P.R. Kersten, Jong-Sen Lee, and T.L. Ainsworth. Unsupervised classification of polarimetric synthetic aperture radar images using fuzzy clustering and em clustering. *Geoscience and Remote Sensing, IEEE Transactions on*, 43(3), 2005.
13. J A Kong, A A Swartz, and H A Yueh. Identification of terrain cover using the optimal terrain classifier. *J. Electronmagn. Waves Applicat.*, 2:171–194, 1988.
14. E Krogager. New decomposition of the radar target scattering matrix. *Electron. Lett.*, 26(18):1525–1527, August 1990.
15. Jong-Sen Lee, Mitchell R. Grunes, Thomas L. Ainsworth, Li-Jen Du, Dale L. Schuler, and Shane R. Cloude. Unsupervised classification using polarimetric decomposition and the complex Wishart classifier. *IEEE Transactions on Geoscience and Remote Sensing*, 37(5):2249–2258, September 1999.
16. Jong-Sen Lee, Mitchell R. Grunes, and R.Kwok. Classification of multi-look polarimetric SAR imagery based on complex Wishart distribution. *International Journal of Remote Sensing*, 15(11):2299–2311, 1994.
17. M. Moakher. Differential geometric approach to the geometric mean of symmetric positive-definite matrices. *SIAM J. Matrix Anal. Appl.*, 26(3):735–747, 2005.
18. Frédéric Pascal, Jean-Philippe Ovarlez, Philippe Forster, and P. Larzabal. Performance analysis of covariance matrix estimates in impulsive noise. *Signal Processing*, 56(6):2206–2216, 2008.
19. Paolo Piro, Frank Nielsen, and Michel Barlaud. Tailored bregman ball trees for effective nearest neighbors. In *European Workshop on Computational Geometry (EuroCG)*, LORIA, Nancy, France, March 2009. IEEE.
20. J J van Zyl and Burnette C F. Bayesian classification of polarimetric SAR images using adaptive a priori probability. *Int. J. Remote Sensing*, 13(5):835–840, 1992.
21. Y.-H. Wang and C.-Z. Han. Polsar image segmentation by mean shift clustering in the tensor space. *Acta Automatica Sinica*, 36(6), 2010.
22. Kung Yao. A representation theorem and its applications to spherically-invariant random processes. *IEEE Transactions on Information Theory*, 19(5):600–608, 1973.
23. H A Yueh, A A Swartz, J A Kong, R T Shin, and L M Novak. Optimal classification of terrain cover using normalized polarimetric data. *J. Geophys. Res.*, pages 15261–15267, 1993.